Applied Surface Science 567 (2021) 150773

Contents lists available at ScienceDirect

Applied Surface Science

journal homepage: www.elsevier.com/locate/apsusc

Full Length Article

Enhanced photocatalytic activity of $BiVO_4$/Pt/PtO_x photocatalyst: The role of Pt oxidation state

Luiz E. Gomes [a,b], Adailton C. Nogueira [a], Marcio F. da Silva [a], Luiz F. Plaça [a], Lauro J.Q. Maia [c], Renato V. Gonçalves [d], Sajjad Ullah [a,e], Sherdil Khan [f], Heberton Wender [a,*]

[a] Nano&Photon Research Group, Laboratory of Nanomaterials and Applied Nanotechnology, Institute of Physics, Federal University of Mato Grosso do Sul, Av. Costa e Silva S/N, 79070-900, Campo Grande, MS, Brazil
[b] Centro de Tecnologias Estratégicas do Nordeste, Av. Prof. Luiz Freire, 01, 50740-540 Recife, PE, Brazil
[c] Grupo Física de Materiais, Instituto de Física, Universidade Federal de Goiás, Goiânia, GO, Brazil
[d] Instituto de Física de São Carlos, Universidade de São Paulo, PO Box 369, São Carlos, SP 13560-970, Brazil
[e] Institute of Chemical Sciences, University of Peshawar, PO Box 25120, Peshawar, Pakistan
[f] Institute of Physics, Federal University of Rio Grande do Sul (UFRGS), Campus do Vale: Av. Bento Gonçalves, 9500 – Agronomia, Porto Alegre, RS, Brazil

ARTICLE INFO

Keywords:
$BiVO_4$
Photocatalysts
Cocatalysts
Platinum oxide
Photocatalytic degradation

ABSTRACT

Monoclinic bismuth vanadate (BVO) has gained attention as a low-cost and promising visible light photocatalyst but suffers from fast charge carrier recombination. The present study reports the controlled photoreduction deposition of different Pt-based co-catalysts on the surface of BVO to address this drawback and brings a detailed discussion on the role of the oxidation state of Pt in determining the photoactivity of the photocatalysts. Results evidenced the presence of both metallic Pt and Pt oxides on the surface of BVO, with proportions that depended on the photoreduction time. The photocatalytic activity towards degradation of three model dyes revealed that platinum oxides (PtO_x, x = 1 or 2) or a mixture of Pt^0/PtO_x species act out as better cocatalysts than Pt^0, with an almost 4-fold higher apparent quantum yield for the optimized sample. The enhanced photoactivity of BVO/Pt/PtO_x photocatalysts was attributed to their improved visible light absorption and enhanced charge carrier separation than pristine BVO or BVO/Pt. This study provides important insight into and a better understanding of the general photodeposition strategy employed to prepare semiconductor/metal (photo)catalysts on one hand and highlights the role of the oxidation state of deposited metal in determining the properties of composite (photo)catalysts on the other.

1. Introduction

The rapid growth in the global population and corresponding unrestrained growth in industrial and agriculture sectors have constantly been perturbing our natural biosphere, leading to serious problems of environmental pollution, particularly water pollution [1]. This has not only resulted in scarcity or unavailability of potable water to a large portion of the world population but is also responsible for the speared of serious water-borne diseases [2]. Various classical and advanced water treatment methods have thus been developed to combat this serious problem of water pollution [3]. Among these, advanced oxidation processes (AOPs); particularly heterogeneous photocatalysis based on semiconductors [4,5], have attracted great attention. The most widely used wide bandgap semiconductor photocatalysts (TiO_2, ZnO), however, require UV light for their photoexcitation, which represents only 3–5% of the solar spectrum, thus limiting the practical utility of heterogeneous photocatalysis [5,6]. For effective utilization of natural sunlight as an abundant source of energy, a great deal of research has been dedicated to the development of new photocatalytic materials that can absorb a wider portion (UV-to-NIR) of the solar spectrum [7-9] and/or to the improvement of photoactivity of the already existing photocatalysts [10-13]. Of particular interest is the development of visible-light-driven photocatalysts [10,13-21] such as $BiVO_4$, CuO, Bi_2MoO_6, MoS_2, CdS, Ag_3PO_4, WO_3, among others that may allow the implementation of solar light-driven photocatalysis as a practical and viable solution to the real-world problem of environmental pollution. Recently, bismuth-based compounds such as $BiVO_4$, $CuBi_2O_4$, Bi_2S_3, Bi_2MoO_6, BiOBr, and $BiFeO_3$ have been extensively investigated [13,15,22-24],

* Corresponding author.
E-mail address: heberton.wender@ufms.br (H. Wender).

https://doi.org/10.1016/j.apsusc.2021.150773
Received 22 March 2021; Received in revised form 28 June 2021; Accepted 26 July 2021
Available online 29 July 2021

among which $BiVO_4$ [12,15,22,25], a ternary metal oxide has stood out high for being one of the most promising visible light photocatalysts for oxygen evolution [11,12], CO_2 reduction [26] and photodegradation of organic and emerging pollutants [11,12,27]. These applications of $BiVO_4$ stem from its promising photocatalytic activity, excellent visible light absorption, low toxicity, low cost, and chemical stability [12,22].

$BiVO_4$ has three main crystalline structures: monoclinic scheelite (ms), tetragonal zircon (tz)-type, and tetragonal scheelite (ts) [28,29]. The ms-$BiVO_4$ structure consists of Bi coordinated by eight O atoms (forming BiO_8 dodecahedron) and V atoms coordinated by four O atoms (forming a VO_4 tetrahedron). Each O atom in the structure is then bonded to two Bi and one V atoms, thus holding the Bi and V centers together, forming a 3D structure [29]. The oxidation states of its three-elements are Bi^{3+} ($5d^{10}$ $6s^2$), V^{5+} ($3d^0$) and O^{2-} ($2p^6$). Moreover, the valence band (VB) in ms-$BiVO_4$ is formed by the O 2p coupled to Bi 6s states, while the conduction band (CB) is formed by the V 3d states with contributions of O 2p and Bi 6p states. On the other hand, the VB in the ts-$BiVO_4$ structure is formed only by the O 2p states.

Despite the good visible-light photocatalytic activity reported for ms-$BiVO_4$ [7], it carries certain limitations such as low electron mobility and high recombination rate of charge carriers (e^-/h^+) which restrict its efficiency [28,30]. To address these fundamental limitations and further improve the photocatalytic activity of $BiVO_4$, different strategies including morphological/facets control, heteroatom/defect doping, co-catalysts deposition, and construction of heterojunction with other semiconductors has been recently explored [10,12,15,29].

The deposition of noble metals on semiconductor particles has been reported to improve their photocatalytic efficiencies [10,31,32]. The enhancement in photoactivity of $BiVO_4$ upon metal deposition results from the fact that the Fermi level of the latter is generally lower than the CB of the semiconductor. This allows the flow of photoexcited electrons from the CB of the semiconductor to the surface-deposited metal, leaving the holes in the VB of semiconductors free for efficient oxidation of organic molecules. Metals with large work functions (such as platinum) serve well as a sink for the photoexcited electrons coming from the CB of the semiconductor and thus is an ideal cocatalyst for the construction of efficient semiconductors/Pt photocatalytic assemblies [33-35].

Among the various methods available for deposition of metal/metal oxides, photoreduction of metal ions/complexes on the surface of $BiVO_4$ is preferable as it allows control of the deposition and loading of metal/metal oxides on its surface by simply controlling the time of irradiation or metal precursor concentration [36,37]. Though several studies have reported the formation of Pt^0 as a result of photoreduction of Pt-based salts on a semiconductor surface (for instance, TiO_2) [38,39], reports and proper characterization of photodeposited Pt species over BVO surface are scarce [40-42]. Moreover, little attention has been paid to the presence of different Pt species with varying oxidation states and the role they play in determining the photocatalytic performance of the Pt/photocatalyst systems. A deeper discussion of the oxidation state of Pt in BVO/Pt composite photocatalysts is essential to properly understand the composition-photoactivity relationship. The present study reports the controlled photodeposition of different Pt species ($Pt^0/Pt^{4+}/Pt^{2+}$) on the surface of m-$BiVO_4$ and the role of the Pt oxidation state on the photoactivity of the $BiVO_4/Pt/PtO_x$ photocatalysts, as measured by photooxidation of three model organic pollutants (methylene blue (MB), methyl orange (MO), and Rhodamine B (RhB)).

2. Experimental

2.1. Chemicals

Bismuth(III) nitrate pentahydrate ($Bi(NO_3)_3{\cdot}5H_2O$, 98%), ammonium metavanadate (NH_4VO_3, 99%), and chloroplatinic acid hexahydrate ($H_2PtCl_6{\cdot}6H_2O$) were purchased from Sigma Aldrich (Brazil) and Methyl Blue (MB) from Vetec, Brazil. All reagents were used without additional purification.

2.2. Synthesis of BVO nanoflakes

We synthesized the BVO powders as previously reported by our group [43]. Briefly describing, 8 mmol of $Bi(NO_3)_3{\cdot}5H_2O$ and 8 mmol of NH_4VO_3 were separately dissolved in 11 mL aqueous solution of HNO_3 (2.0 M) and 19,8 mL of NaOH solution (2.0 M), respectively. Firstly, these solutions were kept under sonication for 30 min (UltraCleaner® 1400A 40 kHz) and, in sequence, magnetically stirred for another 30 min. After complete solubilization, the $Bi(NO_3)_3$ solution was dropwise added into NH_4VO_3 solution under stirring and a yellow suspension was obtained. This suspension was magnetically stirred for 150 min, followed by its pH adjustment to 5.5. The reaction mixture was transferred into a 110 mL Teflon-lined stainless-steel autoclave and carefully sealed. The hydrothermal reaction was performed inside an oven at 140 °C for 6 h with a heating rate of 5 °C min^{-1}. After cooling down to room temperature, the final precipitate was centrifuged at 4500 rpm for 15 min and then washed four times with deionized water and once with ethanol. The obtained yellow powder was dried at 60 °C for 12 h under ambient conditions.

2.3. Preparation of the BVO-Pt

Platinum (Pt)-based nanoparticles were deposited onto BVO *via* a photoreduction method. Briefly, 234 mg of the as-synthesized BVO were added to a beaker containing 250 mL of a 10% (v/v) water/methanol solution. In this case, methanol is added to scavenge the photogenerated holes leaving more electrons available for the reduction of the oxidized platinum species. Different Pt loadings (0.5, 0.75, and 1% Pt (w/w)) on BVO were achieved by adding an amount of H_2PtCl_6 (0.1 M) to the reaction mixture followed by irradiating with a 150 W Hg vapor lamp for 90 and 480 min. A visual change in the color of BVO from yellow to green is observed after photodeposition of Pt-based particles on its surface. All samples were washed three times with water and dried for approximately 12 h for the complete evaporation of the solvents.

2.4. Characterization

The morphology and size of the pristine BVO and BVO-Pt were studied using a Zeiss–Sigma scanning electron microscope equipped with a field emission gun (FEG-SEM) and a high-resolution transmission electron microscope (JEOL – JEM 2100F), equipped with a field-emission gun and operated at 200 kV. X-ray powder diffraction (XRD) patterns, in the range $20 \leq 2\theta \leq 80$ and with an angular step of 0.02° and counting time of 5 s per step, were obtained using a Bruker X-ray diffractometer employing Cu Kα radiation. The surface chemical composition of the samples was studied by X-ray photoelectron spectroscopy (XPS) using a conventional XPS spectrometer (Scienta Omicron ESCA+) equipped with a high-performance hemispheric analyzer (EAC2000) and monochromatic Al Kα ($h\nu = 1486.6$ eV) radiation as the excitation source. The operating pressure in the ultra-high vacuum chamber (UHV) during the analysis was 10^{-9} Pa. The high-resolution XPS spectra were recorded at constant pass energy of 20 eV with 0.05 eV per step. UV–Vis diffuse reflectance spectra of the powders were obtained using a LAMBDA 650 UV–Vis spectrometer (PerkinElmer) equipped with an integrating sphere and were transformed to absorption spectra by the Kubelka–Munk method. The Raman spectra were recorded by a Raman spectrometer (SCIAPS, Advantage 532), using a 532-nm laser source for excitation. Steady-state photoluminescence (PL) spectra were recorded under 375 nm excitation using a Fluorolog-3.11 spectrofluorometer (Horiba Jobin Yvon, Paris, France) equipped with a 450 W ozone-free xenon lamp and a photomultiplier detector sensitive in the range of 200–850 nm. The time-resolved PL was measured by the time-correlated single-photon counting technique (Horiba Jobin Yvon, Paris, France) using the excitation of a Horiba NanoLED-390 at 390 ± 10 nm peak wavelength and pulse width <1.2 ns. Electrochemical impedance spectroscopy (EIS) was performed using an AutoLab® potentiostat/

galvanostat, with a standard three-electrode system. The photoelectrode preparation was carried by sonicating 4 mg of the as-prepared BVO (or BVO-Pt) powders in 2 mL of H_2O containing 80 μL of Nafion solution (5 wt%) and then drop-casting 200 μL of catalyst ink directly onto a limited area of 1 cm^{-2} of pre-cleaned fluorine-doped tin oxide (FTO) glass substrate. These films were used as the working electrode in a three-electrode configuration electrochemical cell, while a saturated calomel electrode was used as the reference electrode and a platinum wire as the counter electrode. A 0.5 M Na_2SO_4 solution (pH 6.6) was used as the electrolyte. EIS measurements were conducted with frequencies varying from 40 mHz to 100 kHz, the amplitude of 10 mV, and applied potential set as 0 V vs. the open circuit potential (OCP), under dark conditions. The Mott–Schottky (M–S) analyses were obtained by ranging the applied potential from −0.8 to 0.4 V at 1000 Hz.

2.5. Evaluation of photocatalytic activity

The photocatalytic activity of BVO and BVO-Pt samples was evaluated through the photodegradation of selected azo dyes (MB, MO, and RhB). Initially, in each experiment, 25 mg of the photocatalyst were dispersed in 25 mL aqueous MB solution (10 mg L^{-1}). Before irradiation, the photocatalyst/dye suspension was magnetically stirred under dark for 30 min to allow dyes adsorption on the photocatalyst and achieve adsorption–desorption equilibrium. Subsequently, the suspension was irradiated using a solar simulator (Abet Tech model 10500), equipped with a 150 W xenon lamp and an AM1.5G filter for ensuring the reproducibility of the solar spectrum. The system was calibrated for irradiating approximately 300 mW cm^{-2} by using an Abet Tech calibration cell (model 15151). The suspension was kept under magnetic stirring during the illumination and aliquots of 300 μL were collected at intervals of 5 min and centrifuged to remove the photocatalyst for analysis of the supernatant by UV–Vis spectroscopy. A scheme of the experimental setup used for the photocatalytic experiments is presented in Fig. S1. All experiments were carried out in triplicate. Once the best sample was determined, the photodegradation of MO and RhB was also studied under the same experimental conditions. The percentage degradation of each dye was calculated based on the decrease in the intensity of the peak of maximum absorption (λ_{max} of 664, 553, and 464 nm for MB, RhB, and MO, respectively) in the corresponding electronic absorption spectra of the dye.

The apparent quantum efficiency was calculated using previously reported procedures by our group [16,18]. To obtain quasi-monochromatic radiation at 420 nm, a 50 W blue light-emitting diode (LED) lamp ($\lambda = 420 \pm 10$ nm) was used. The irradiance (E) measured under these conditions was 1330 Wm^{-2} and was converted into photon flux (E_{QF}) using the following relationship [16,18]:

$$E_{QF} = E \times \lambda \times 0.836 \times 10^{-2} = 4669.9 \text{ μmol of photons } m^{-2}\ s^{-1}.$$

The AQE was calculated using the following equation.

$$EQA = \frac{photodegraded\ \ molecules\ \ [\text{mol}\ m^{-2}\ s^{-1}]}{E_{QF}\ \ [\text{mol}\ m^{-2}\ s^{-1}]} \times 100$$

The numerator in the above equation was obtained by monitoring the light absorption peak of the MB located at 664 nm. For this, the absorbance value was converted to concentration (mol m^{-2} s^{-1}) after using a calibration curve obtained with different MB concentrations and by considering the focused area of the incident light of $\pi \times 10^{-4}$ m^2, measured at the position of the liquid surface.

3. Results and discussion

3.1. Characterization

The crystalline features of the pristine BVO sample were investigated by XRD analysis. The X-ray diffraction pattern and the respective Rietveld refinement are shown in Fig. 1a.

The narrow diffraction peaks of the sample matches that of the monoclinic scheelite phase (ICSD file 01751866), indicating the formation of well–crystalline ms-BVO, with a unit cell belonging to the spatial group I112/b, with refined cell parameters of a = 5.18 Å, b = 5.08 Å, c = 11.67 Å, α = β = 90° and γ = 90.36° and a preferential orientation along with {0 4 0} facets, in accordance to the literature [43-45]. As expected, the XRD peaks of Pt-deposited BVO samples were identical to that of pristine BVO due to the low Pt content under the detection limit of the equipment. The results extracted from the Rietveld refinement are summarized in Table S1 and Fig. S2. Through the unit cell (Fig. S2), it can be seen that each V atom is coordinated by four O atoms forming a VO_4 tetrahedron, while each Bi atom is coordinated by eight O atoms constituting a BiO_8 dodecahedron, as reported in the literature [46]. Besides, some Bi and O vacancies were included for the best fitting, as presented in Table S1 and Fig. S2.

Raman spectroscopy analysis was performed to probe the structure of BVO and BVO/Pt (Fig. 1b). Four peaks were observed in all Raman spectra, all of which correspond to the ms-BVO [7,47] despite the presence of photodeposited platinum either by photoreduction during 90 or 480 min. The highest intensity Raman band around 827 cm^{-1}, which is sensitive to changes in the local structure of BVO, is assigned to the symmetrical stretching mode (ν_s) of the V–O bond. A closer inspection of this band shows a slight shift to a higher wavenumber region correlated to a change of V–O bond when Pt species are deposited on BVO and lies at 830.2 cm^{-1} for the BVO-Pt(480 min) sample. This indicates a slight change in the local structure of BVO after Pt photoreduction and a close contact or interaction between the two components of the composite photocatalysts. Furthermore, the length (L) of V—O bond calculated based on the Raman stretching frequency (ν (cm^{-1})) using the formula $\nu\ [cm^{-1}] = 21349 \exp(-1.9176L\ [Å])$ [48] was found to be 1.695 Å and 1.693 Å for BVO and BVO/Pt(480 min) samples, respectively. Such a blue shift in the Raman band position has also been previously observed for gold-loaded TiO_2 films and surface-active agent coated TiO_2 nanoparticles and assigned to local lattice distortions at the Au/TiO_2 interface in the former case [49,50]. It is well-known that the surface atoms of nanoparticles (BVO in this case), with somewhat lower coordination number or missing neighboring atoms, are bound by weak forces and show vibration at lower wavenumbers as compared to atoms present inside the particle surface. Photoreduction of Pt on the surface of BVO may slightly change the surface energies and bonding situation/interactions, possibly producing compressive stress, leading to somewhat tighter packing and hence a blue shift of the corresponding Raman bands to high wavenumber [50], in corroboration with a slight decrease in the V—O bond length. The other three Raman bands at 708, 366, and 325 cm^{-1} are attributed to the asymmetric stretching mode (ν_{as}) of the V—O bond, and the asymmetric (δ_{as}) and symmetric (δ_s) angular deformation modes of the V—O in VO_4^{3-} tetrahedrons, respectively [47]. The other two characteristic Raman bands of ms-BVO, which are expected at around 213 and 129 cm^{-1} and refer to the rotation and translation modes respectively [51], could not be observed due to the operational limit of the equipment used.

The morphology of the BVO and BVO/Pt was evaluated to understand the nature and size of the platinum-based particles photodeposited on the surface of BVO, as shown in Fig. S3. As a result, FEG-SEM images of BVO show irregular branch-shaped particles, with an estimated average size of 204 ± 66 nm, as obtained before [43]. After Pt photodeposition, HRTEM images confirmed the formation of <10 nm Pt-based NPs on the surface of BVO (Fig. S3). Besides, the observed interplanar distances of 0.28 nm and 0.33 nm may be attributed to the (0 0 4) planes of the ms-BVO (ICSD file no. 01751866) and the (1 1 0) planes of orthorhombic PtO_2 (ICSD file no. 431045), respectively, as a first indication that the Pt content was not fully reduced to Pt^0.

The XPS characterization of pristine BVO confirmed the presence of V^{5+} and Bi^{3+} in this sample (see Fig. S4 and Table S2 for more details). Besides, we carefully analyzed the O 1s region (Fig. S5 and S4b) and Pt

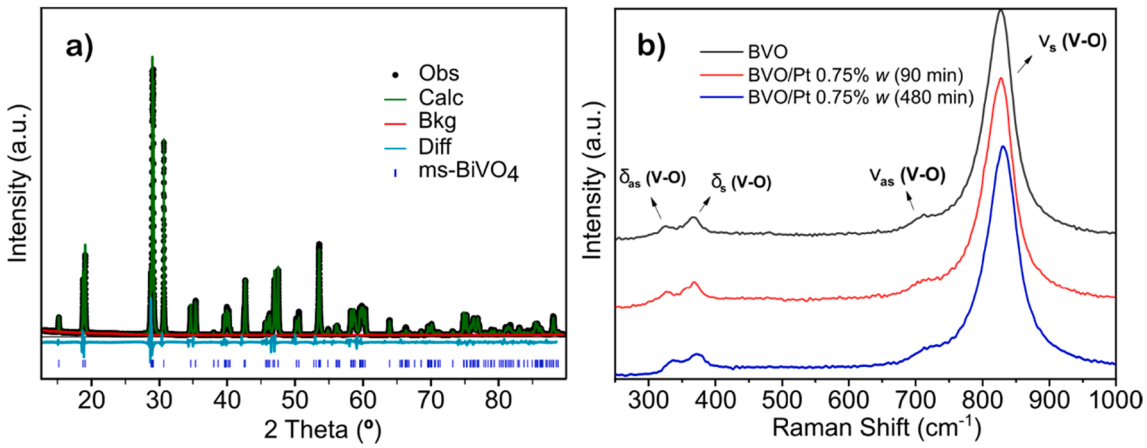

Fig. 1. (a) XRD pattern and Rietveld refinement of the pristine BVO sample; (b) Raman spectra of BVO and BVO/Pt 0.75% samples.

4f regions (Fig. 2) using high-resolution XPS to better characterize the Pt oxidation states.

The Pt 4f high-resolution spectra revealed two main components due to the spin–orbit coupling, namely Pt $4f_{7/2}$ and Pt $4f_{5/2}$, as expected. For BVO/Pt 0.75% (90 min) sample (Fig. 2a), adequate peak-fitting of the high-resolution spectra could be done considering three different oxidation states for Pt. The three Pt $4f_{7/2}$ components located at 74.84, 72.83 and 71.21 eV (Table 1) could be attributed to PtO_2 (38.79 %), PtO (50.78%) and Pt^0 (10.43%), respectively [39,52]. We could not observe any characteristic photoemission peaks in the expected Cl 2p region, excluding the possible presence of $PtCl_6^{2-}$ and/or $PtCl_4^{2-}$ ions on the surface of BVO. XPS analysis thus suggests the presence of both Pt^0 and PtO_x on the surface of the BVO/Pt 90 min sample.

For the higher photodeposition time (480 min), the same three oxidation states (Pt^{4+}/Pt^{2+}/Pt^0) were considered, with their corresponding Pt $4f_{7/2}$ components located at 74.70 eV, 72.28 eV, and 70.41 eV. As expected, the relative amounts of the different Pt species change upon longer irradiation [39,52,53] and were found to be 2.06% (PtO_2), 25.55% (PtO), and 72.39% (Pt^0) (Fig. 2b and Table 1). It turns out that the increase in photoirradiation time results in the formation of a larger amount of Pt^0, accompanied by a sharp decrease in the proportion of oxidized Pt and, for the BVO/Pt 0.75% (480 min) sample, Pt^0 is the dominant specie, though a complete photoreduction of H_2PtCl_6 to Pt^0 could still not be achieved. These assumptions were validated by the O 1s high-resolution spectra analysis (Fig. S5 and Table S3). The values of the binding energies and percentages of area of each Pt $4f_{7/2}$ component are reported in Table 1. Hereafter, the BVO/Pt samples will be named BVO/Pt/PtO_x since they present a mix of different platinum oxidation states.

Table 1
Values of binding energy and peak area of Pt $4f_{7/2}$ components obtained by XPS before and after MB photodegradation under simulated solar irradiation.

Species	BVO/Pt/PtO_x 0.75% 90 min		BVO/Pt/PtO_x 0.75% 480 min	
	Binding energy (eV)	Area (%)	Binding energy (eV)	Area (%)
Before MB photodegradation				
Pt^0	71.21	10.43	70.41	72.39
Pt^{2+}	72.83	50.78	72.28	25.55
Pt^{4+}	74.84	38.79	74.74	2.06
After MB photodegradation				
Pt^0	70.61	35.55	70.97	95.46
Pt^{2+}	72.21	53.54	72.93	4.54
Pt^{4+}	74.63	10.91	–	–

The optical properties of BVO and BVO/Pt/PtO_x samples were studied by DRS measurements in the visible region. The absorbance-transformed DRS spectra and the corresponding Tauc-plots are shown in Fig. 3.

For BVO, the absorbance dramatically drops around 500 nm which is a characteristic feature of the semiconductor band edge (Fig. 3a). The indirect bandgap of pristine BVO before and after Pt/PtO_x NPs photodeposition was estimated from the Tauc Plots [16,18] as ~2.4 eV

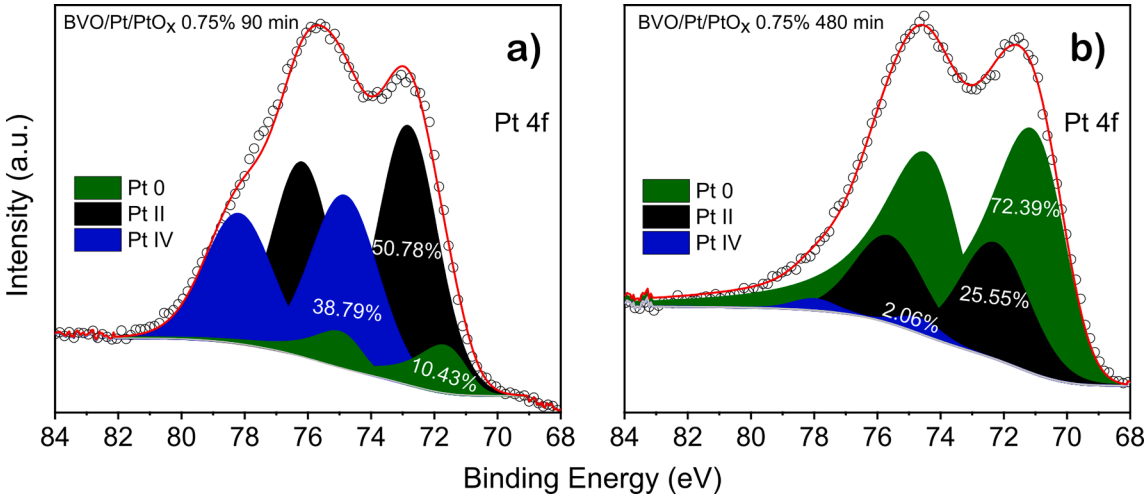

Fig. 2. Pt 4f high-resolution XPS spectra of (a) BVO/Pt 0.75% (90 min) and (b) BVO/Pt 0.75% (480 min) samples.

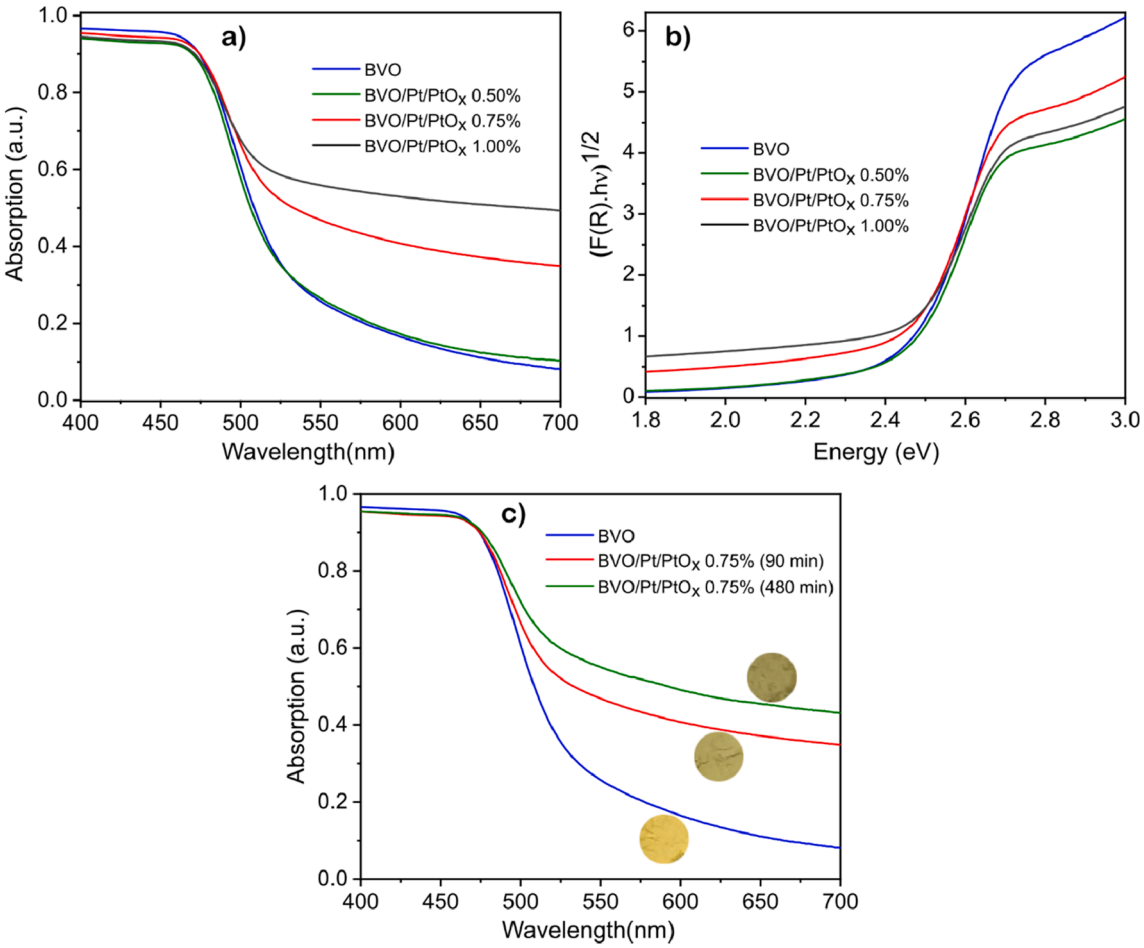

Fig. 3. (a) Absorption-transformed DRS spectra of BVO and BVO/Pt samples (photoreduced for 90 min) and (b) their corresponding Tauc-Plots obtained by considering BVO as an indirect bandgap semiconductor. (c) Comparison of the absorption spectra of BVO and BVO/Pt/PtO_x samples photoreduced for 90 and 480 min.

(Fig. 3b, Fig. S6), in accordance with the reported bandgap for ms-BVO [54]. In addition, the bandgap of BVO did not change upon Pt/PtO_x NPs photodeposition for 90 and 480 min (Fig. 3b) and suggests that the NPs were only deposited on the surface of BVO and should work as co-catalysts. Moreover, the BVO light absorption extended through the entire visible region with a non-zero absorption even at 700 nm (Fig. 3a and c), which has been previously related to structural defects [55]. Upon deposition of Pt/PtO_x NPs, the light absorption in the 500–700 nm wavelength region increased significantly, in corroboration with yellow-to-greenish color change observed after the photodeposition process (Fig. 3c inset). In fact, the higher the amount of platinum deposited or the longer the photoreduction time, the greater is the light absorption in the 500–700 nm region. It shows that the gain in visible light absorption scales with the increase of metallic platinum.

3.2. *Photocatalytic activity of the BVO and BVO/Pt/PtO_x*

The photocatalytic activity of pristine BVO and BVO/Pt/PtO_x samples (photoreduced for 90 min, unless another value is indicated) with different Pt content was first studied through the photodegradation of the MB dye (Fig. 4a). Clearly, the MB concentration has not changed much with the irradiation time in the absence of photocatalysts. Pristine BVO could photodegrade around 50% of MB in 30 min, with a photoactivity overperformed by the Pt-deposited samples. For instance, after 10 min of irradiation, the BVO containing 1.0% and 0.75% of Pt, and the pristine BVO photocatalysts could photodegrade 100%, 98%, and 35% of the MB dye, respectively. The effect of Pt loading on BVO is evident from a comparison of the pseudo-first-order kinetic constants (k) of dye removal in the presence of BVO and BVO/Pt/PtO_x samples (Fig. 4b). The kinetic constant increased by a factor of 8.7 in going from pristine BVO ($k = 0.03\ min^{-1}$) to BVO/Pt/PtO_x 0.75% ($k = 0.26\ min^{-1}$), showing that the photodeposited Pt accelerates the photodegradation of the MB. The photoactivity of the 1% Pt sample is slightly superior to the 0.75% that could be considered optimal concerning the cost/benefit ratio. Henceforth all additional photocatalytic tests were performed using BVO/Pt/PtO_x 0.75% sample.

Fig. S7a shows the temporal evolution of MB UV–Vis absorption spectra over the BVO/Pt/PtO_x 0.75% photocatalyst, where a blue shift and an intensity reduction in the maximum absorption peak of MB could be seen with the irradiation time. It was accompanied by intensity reduction and red shifting of the two absorption peaks of MB in the UV region, suggesting that most MB has completely decomposed without generating intermediate compounds [56]. Besides, N-demethylation and chromophore cleavage seems to predominate using BVO/Pt/PtO_x photocatalyst [57-59] since they are analogous and competitive photodegradation reaction during the photocatalytic decomposition of organic pollutants being reported to cause a blue shift in its maximum absorption peak. The photoactivity of the BVO/Pt/PtO_x 0.75% photocatalyst was also evaluated through the photodegradation of the other two dyes, namely MO and RhB, under simulated solar irradiation (Fig. 4c), where the respective dyes maximum absorption peaks of RhB also blue-shifted during the photocatalytic experiments (Fig. S7). Direct photolysis of the dyes by light (in absence of photocatalyst) was negligible however a high photodegradation rate was observed in the

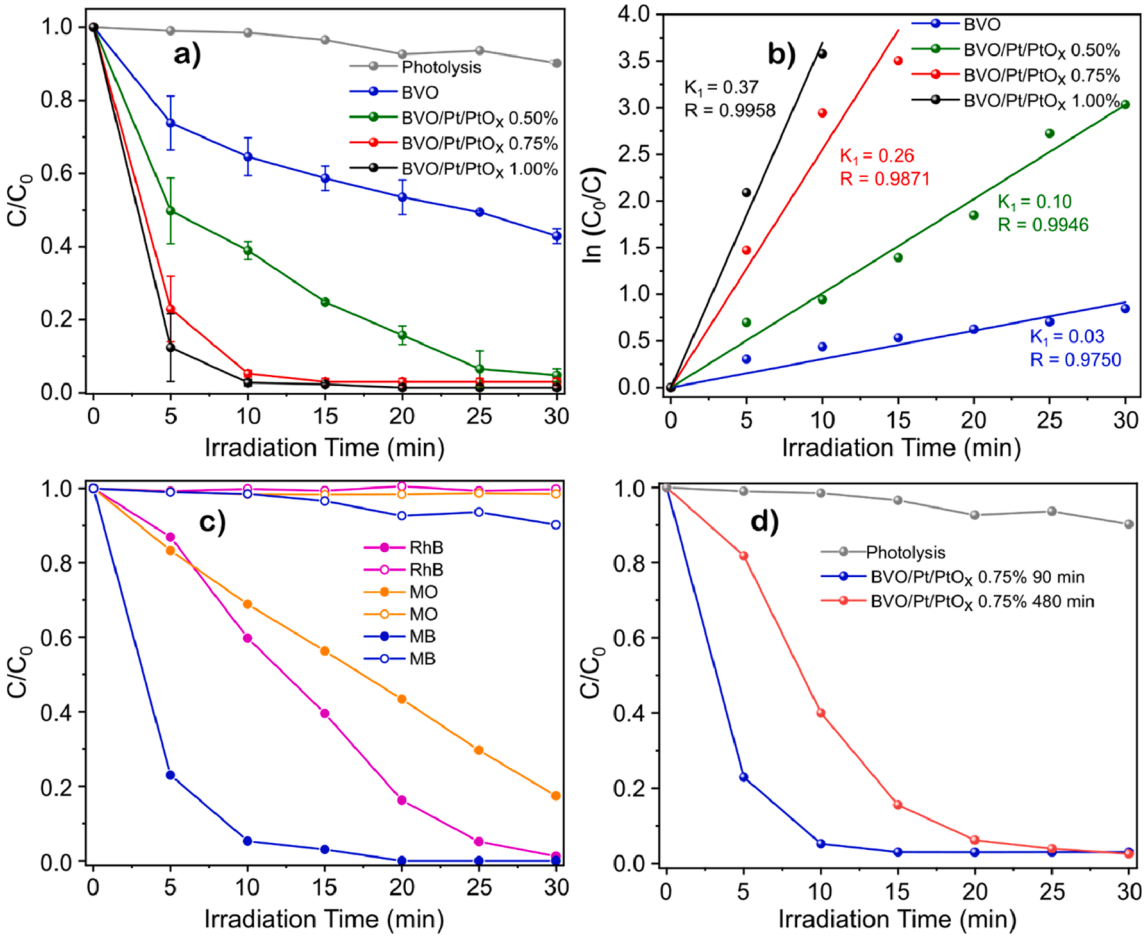

Fig. 4. Photocatalytic experiments under simulated solar irradiation under the following conditions: 300 mW cm^{-2} of irradiance with AM1.5G; 1 mg mL^{-1} of photocatalysts and 10 ppm dye solution. (a) C/C_0 curves of the photocatalytic degradation of MB solution using BVO and BVO/Pt/PtO_x samples. (b) Pseudo-first-order kinetic plot of MB solution degradation in the presence of BVO and BVO/Pt/PtO_x samples, where (k_1) is the pseudo-first-order kinetic constant and R is the correlation coefficient of the linear fit. (c) C/C_0 curves of the different dyes using BVO/Pt/PtO_x 0.75% 90 min photocatalyst, where open circles represent the direct photolysis of the corresponding dye. (d) Comparison of photocatalytic activity for MB removal using BVO loaded with Pt-based cocatalysts photoreduced for 90 and 480 min.

presence of the photocatalyst in the order MB > RhB > MO. The faster photodegradation of the cationic dyes (RhB and MB) possibly arises from their increased electrostatic attraction to the negatively charged surface of the photocatalyst (Zeta potential measured at -16.6 ± 0.6 mV). Furthermore, the difference in photoreactivity between MB and RhB could be related to the smaller size (and hence lesser steric hindrance) of the former [60] and/or to the fact that molecules of the latter may be cationic or neutral (depending on whether the carboxylic acid groups are deprotonated or not) which, in the last case, may interact weakly with the photocatalyst's surface.

Though several studies have reported the formation of Pt^0 through photoreducing Pt-based salts on a semiconductor surface, reports on the preparation of BVO/Pt materials are fewer and little attention has been paid to the presence and effects of different Pt species with varying oxidation states [40-42]. A deeper discussion of the oxidation state of Pt in BVO/Pt photocatalysts is essential to properly understand their composition-photoactivity relationship. In fact, the presence of oxidized Pt species (PtO and/or PtO_2), in addition to metallic (Pt^0), has been detected in TiO_2/Pt samples prepared through photoreduction of Pt-based salts [38,39] in the presence of TiO_2. Our results show that the photodeposition of H_2PtCl_6 onto the BVO surface for 90 min ends up in the formation of a mixture of PtO_2, PtO, and Pt NPs. To obtain samples with a higher Pt^0 to $Pt^{2+/4+}$ ratio and thus study the influence of the amount of oxidized Pt on the photoactivity of BVO, the photoreduction process was performed for a longer time (480 min). Fig. 4d shows a comparison of the photocatalytic activity of the BVO loaded with Pt-based cocatalysts photoreduced for 90 and 480 min. It is noteworthy that both samples could almost completely photodegrade the MB dye within 25 min of simulated solar irradiation, however, with different kinetic behaviors where a much faster reaction could be observed for the 90 min samples. It turns out that a higher content of Pt^0, as observed by XPS for the 480 min sample, was detrimental to the photocatalytic activity of the BVO/Pt/PtO_x photocatalytic system. Reusability of the best photocatalyst was investigated against MB photodegradation and a slight decrease in the photoactivity could be observed (Fig. S8) due to photoreduction of the oxidized Pt species and/or formation of more Pt^0 particles. However, it is important to highlight that in our experiments the photocatalysis is fast and almost all the MB decolorized after the first 15 min of photoirradiation. Therefore, the irradiation dose during a whole photocatalytic run is not so high, and even after three consecutive runs the MB total removal diminished from 98% (first run) to only 93% (third run), showing that the photocatalysts can be recycled several times without a substantial loss in efficiency.

At this point, the reader may be concerned about the photosensitization effect since many dyes can inject electrons into the CB of a semiconductor when photoexcited, which could throw any semiconductor-based photocatalytic mechanism down, as warned by previous studies [61]. In fact, this is sometimes the problem when discussing the photocatalytic activity of semiconductors without due care regarding all possibilities that can impact the chemical reactions. To

investigate the presence of a possible sensitization effect, we show in Fig. 5 the photoactivity of BVO and BVO/Pt/PtO_x samples by using an LED light source irradiating at 420 ± 10 nm, specially chosen because in this particular range the MB dye cannot absorb photons (Fig. S7). Therefore, under these conditions, only the semiconductor can act as the absorber material. After five minutes of irradiation with this LED setup (1330 W m^{-2} @420 nm), the BVO/Pt/PtO_x photocatalyst could completely degrade the MB dye, meanwhile, the BVO removed 65% of the dye and the photolysis effect accounted for only 6% removal. This result guarantee that the semiconductor is the main absorber material and photosensitization is not an issue since MB does not absorb photons at 420 nm [18,62,63]. Fig. 5b shows the value of the pseudo-first-order kinetic constants (k) for MB removal in the presence of BVO and BVO/Pt/PtO_x photocatalyst. The kinetic constant of pristine BVO is 0.021 min^{-1} against 1.21 min^{-1} for BVO/Pt/PtO_x, showing that the photodeposited Pt accelerated MB removal by an impressive factor of ~58 folds under LED irradiation. It is to note that the same experiment ended in a 10-fold increase for the kinetic constant when using simulated solar light.

The apparent quantum efficiency (AQE) of the BVO/Pt/PtO_x photocatalyst was estimated under LED irradiation (Fig. 5c). AQE measurements are important because it gauges the photocatalytic activity based on the number of incident photons and the illuminated area, and therefore can be compared with other measurements carried out in different laboratories, provided that proper experimental care is taken. It is noted that the AQE for pure BVO is small (0.024%), however, with the addition of the Pt/PtO_x cocatalysts, AQE showed a 3.8-fold increase (0.091%). It is expected an AQE decrease as the reaction time proceeds as the degradation follows an exponential decay law with the time of irradiation, i.e., higher amounts of the dye are degraded at the very beginning of the reaction. In fact, our results show that the AQE of BVO/Pt/PtO_x decreased from 0.091 to 0.067 and, soon after to 0.049%, considering the irradiation times of 1, 2, and 3 min, respectively. Moreover, the AQE decrease with irradiation time is higher for the Pt-containing samples which may be due to the increase in the content of Pt^0 during the photoirradiation, as will be discussed later.

3.3. Discussion of the improved photoactivity mechanism

To better understand the photocatalytic behavior of the samples, XPS characterization before and after the MB photodegradation experiment was performed. Fig. S5 and Fig. 6 respectively present the high-resolution spectra of the O 1s and Pt 4f regions after the MB photodegradation experiments for the samples photoreduced by 90 and 480 min.

XPS analysis of the recovered BVO/Pt/PtO_x 90 min (Fig. 6a, Table 1) after the MB photodegradation test showed the presence of Pt^0 (35.55%), PtO (53.54%), and PtO_2 (10.91%) [39,52]. Thus, the PtO_x content decreased with and concomitantly increased Pt^0 content after the photodegradation experiment (see Table 1). Therefore, our results show that the higher the irradiation dose, the smaller is the proportion of oxidized platinum species (Pt^{2+}/Pt^{4+}). Indeed, the BVO/Pt/PtO_x 480 min sample (Fig. 6b) exhibits only two oxidation states after the MB photodegradation test, Pt^0 (95.46%) and PtO (4.54%), with their corresponding Pt $4f_{7/2}$ component located at 70.97 and 72.93 eV, respectively [39,52,53]. This fact is expected since Pt^{4+} was not completely reduced during photodeposition (preparation of BVO/Pt/PtO_x samples), therefore, the reduction process of the remaining oxidized Pt species continues to proceed during the dye photodegradation experiment. This hypothesis is confirmed by the investigation performed on the O 1s region (Fig. S5). Furthermore, the increase of Pt^0 species after photodegradation was followed by an increase in the amount of adsorbed oxygen species (Table S3) which points to an effective dye-photocatalyst interaction important for the photocatalytic activity of the material.

The photoluminescence (PL) technique is a useful tool to study electron/hole (e^-/h^+) recombination in semiconductor materials as the electron decay from an excited state to some lower energy state or ground state results in the emission of PL light [64]. The intensity of emitted PL light depends on the type/structure of materials [65] and the rate of e^-/h^+ recombination, where a lower PL emission intensity (at a fixed wavelength near the absorption band edge) may be indicative of lesser e^-/h^+ recombination [66,67]. PL technique was thus used to elucidate the role of deposited Pt-species in the promotion or inhibition of e^-/h^+ recombination in BVO. Fig. 7a presents the PL emission spectra of the pristine BVO and the BVO/Pt/PtO_x sample obtained under excitation at 375 nm and the excitation spectrum of pristine BVO can be seen in Fig. S9. All samples show a broad PL emission centered at around 520 nm (wavelength close to the BVO absorption edge), suggesting that it results from the recombination of e^-/h^+ in BVO [68,69]. It is important to highlight that electron-hole pairs can recombine by radiative or nonradiative pathways. PL emission bands come from radiative recombination of electron-hole pairs via numerous key routes upon photoexcitation energies higher than the bandgap [64]. The first and primary step involves the successful relaxation of charge carriers to the shallow surface trap states and the bottom of the CB (for the electrons, and top of the VB in the case of holes). The recombination only contributes to band edge emission when photons are emitted, whilst nonradiative decays normally involve charge trapping at defect states within the bandgap [64,70]. One should note that further radiative recombination coming from these trapped charges (donor–acceptor levels) may produce additional emission bands of lower energy than the band edge emission. In our case, we could observe a broad emission band extending up to 580 nm that can be explained by the presence of radiative recombination of trapped charges. In summary, the overall lower PL intensity for BVO/Pt/PtO_x indicates that photogenerated electrons in the excited $BiVO_4$ are transferred to the Pt/PtO_x NPs

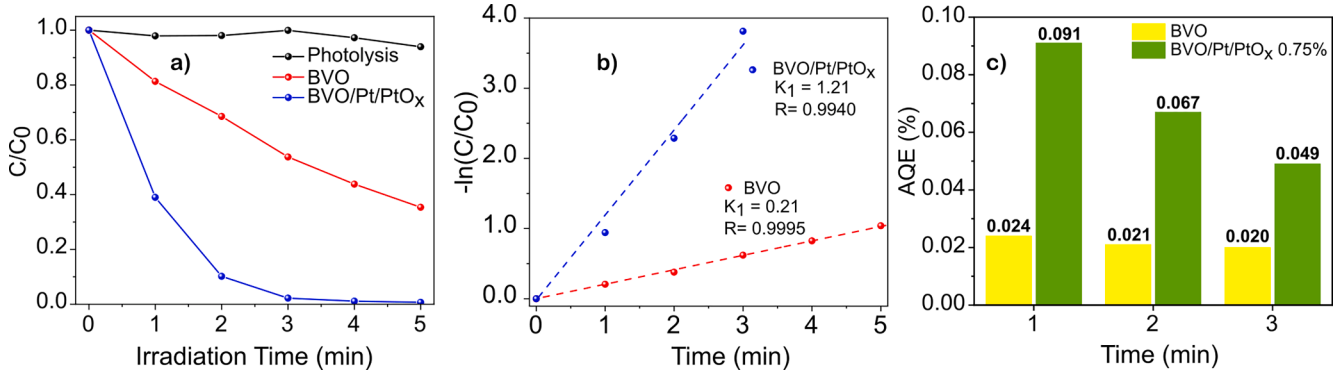

Fig. 5. Photocatalytic experiments using 1 mg mL^{-1} of BVO/Pt/PtO_x 0.75% photocatalyst and 10 ppm dye solution under an LED light source (irradiating at 420 ± 10 nm). (a) C/C_0 curves of MB photodegradation; (b) the respective pseudo-first-order kinetic fit and (c) AQE measurements.

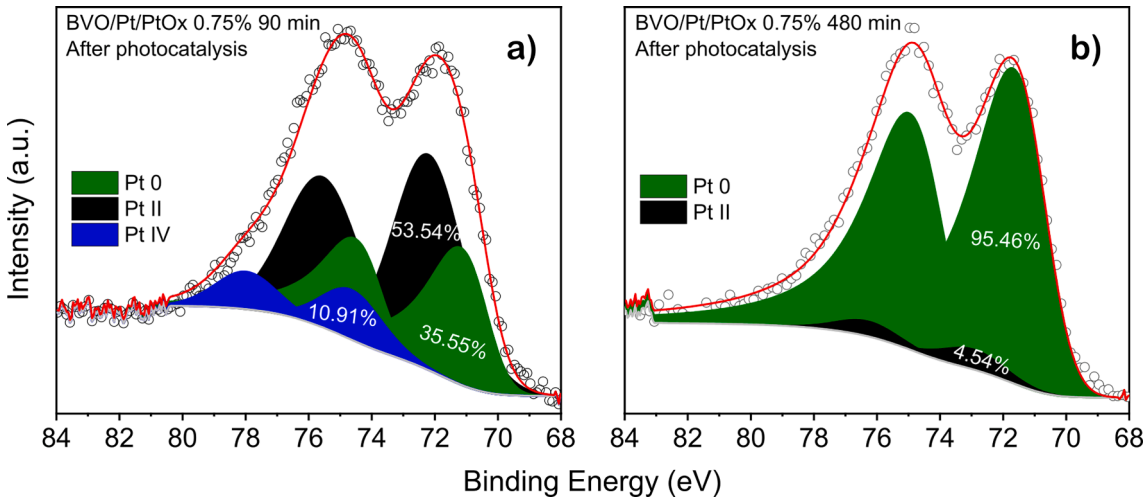

Fig. 6. Pt 4f high-resolution XPS spectra of (a) BVO/Pt/PtO_x 0.75% (photoreduction for 90 min) and (b) BVO/Pt/PtO_x 0.75% (photoreduction for 480 min) samples, recovered after the photocatalytic degradation of MB.

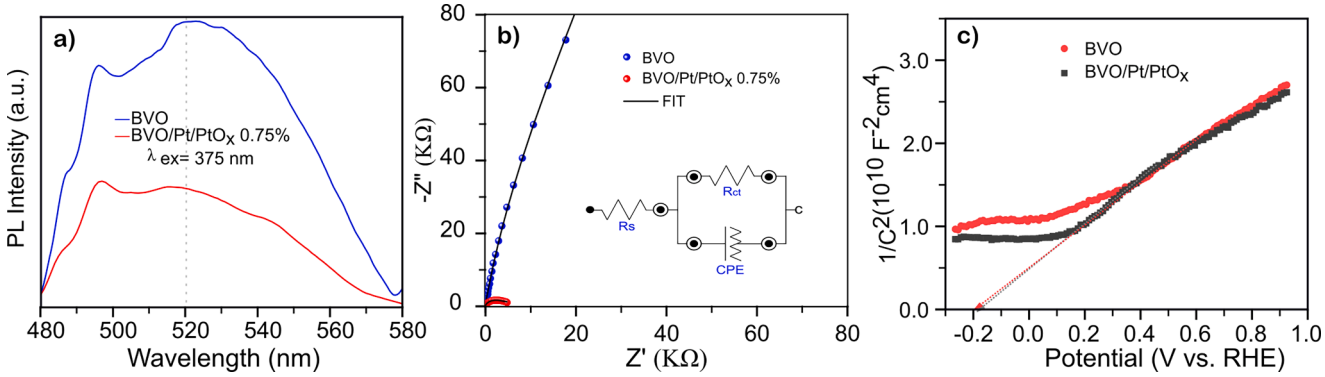

Fig. 7. (a) PL emission spectra under 375 nm excitation and (b) electrochemical impedance spectroscopy measurements of BVO and BVO/Pt/PtO_x 0.75% (90 min) samples under the dark condition; (c) Mott-Schottky plot of the $BiVO_4$ electrodes recorded in the dark at 1000 Hz.

immediately after the photo-production, reducing, therefore, the recombination rate of charge carriers, as also reported for $BiVO_4$-reduced graphene oxide [71], $CeO_x/BiVO_4$:Eu^{3+} NPs [72], Co-doped $BiVO_4$ [67]. Besides, band-edge PL lifetime was studied using the time-correlated single-photon counting technique (Fig. S10). The PL lifetime curves at the nanosecond range could be fitted with two decay times where the fast component is attributed to electron trapping and the slow component is due to electron-hole recombination, as reported before [73]. BVO with and without Pt/PtO_x deposition showed equivalent lifetimes of 5.8 and 12.2 ns for the fast (τ_1) and slow (τ_2) components, respectively. This result suggests that deposition of Pt/PtO_x cocatalysts did not change the lifetime of BVO charge carriers but show that electron-hole recombination was avoided by the efficient charge transfer to Pt/PtO_x NPs.

EIS analyses were performed to study the charge transfer resistance from the semiconductor to the electrolyte and, indirectly, the separation of e^-/h^+ pairs at the electrode surface (Fig. 7b). The radii of the formed semicircles are related to the charge transfer at the interface formed between the semiconductor and the electrolyte, so that the smaller the radius of the semicircle, the lower the resistance of charge transfer [74,75]. The EIS data shows a single semicircular arch for both samples; however, the semicircle referring to the BVO/Pt/PtO_x sample is far smaller than that of pristine BVO, thus indicating a lower charge transfer resistance when Pt/PtO_x is present in the photoelectrode. The EIS data were simulated taking into account the equivalent circuit shown in Fig. 7b (inset), which includes the resistance of the solution (R_S), the charge transfer resistance at the interface between the working electrode and the electrolyte (R_{ct}), and a constant phase element (CPE). The results obtained for the R_{ct} were 928 KΩ and 4.68 KΩ before and after photoreduction of Pt on BVO, respectively, indicating that the Pt deposition considerably decreased the charge transfer resistance of the photoelectrode by a factor of ~200. This represents a considerable reduction for this system since studies reported in the literature for the BVO showed that the R_{ct} decrease between 30 and 70% [76-79]. Therefore, the EIS results corroborate the PL findings, indicating that Pt/PtO_x is working as an efficient cocatalyst on the surface of the BVO, decreasing the recombination of the photogenerated charges and, consequently, improving the photocatalytic activity.

For a further in-depth understanding of the photoactivity performances including the electronic properties of the photocatalysts, we conducted the Mott–Schottky (M−S) analysis to determine the type of conductivity of the system and the flab band potential (V_{fb}), with is close to the CB of n-type semiconductors. Under the M−S analysis, by plotting $1/C^2$ against V (where C is the space charge layer capacitance, and V is the applied voltage), the curve intercept at the horizontal axis provides the V_{fb} of the electrode material, Fig. 7c. The M−S plots of all samples showed positive slopes, indicating that all the photocatalysts are indeed n-type semiconductors, meaning electrons are the majority charge carriers. The V_{fb} of the electrodes is ~−0.2 vs. RHE for both pristine BVO and BVO/Pt/PO_x, showing that deposition of Pt/PtO_x species does not modify the electronic properties of the BVO photocatalyst.

From an analysis of the discussion presented above, it can be inferred

that the presence of high amounts of Pt^{2+} (PtO) and Pt^{4+} (PtO_2) species distributed over the BVO surface improves the photocatalytic performance when compared to pure BVO or even with the case of Pt^0 as the majority Pt specie. Based on these results, a mechanism for the dye's photocatalytic degradation is proposed, as shown in Fig. 8.

Initially, PtO_x NPs (PtO and PtO_2) are deposited on the surface of BVO. These PtO_x NPs act as traps for the photoexcited electrons in the CB of BVO (measured as −0.2 V vs. RHE), getting reduced to form a structure with the reduced Pt-species distributed at the NP outer surface and avoiding recombination of the BVO electron/hole pairs due to the formation of Schottky barrier between Pt^0 species and BVO (Fig. 8). As observed by XPS, the longer the irradiation time the greater the amount of reduced Pt-based species due to the consumption of the photogenerated electrons at the CB of BVO. Besides, the PtO_x is a p-type semiconductor, and a metal/semiconductor junction is also promoted at the NPs interface. Under light excitation, even if to a lesser extent owing to the low content of platinum, electrons are injected from the PtO_x to the Pt^0 and the photogenerated holes are left behind in the VB of PtO_x. Therefore, electrons both coming from the CB of BVO or the PtO_x accumulate at the Pt^0 NPs. At this stage, electrons most probably react with the dye molecules to produce reduced dye species or with adsorbed O_2 to generate $HO_2^{\bullet}$ (E^0 ($O_2/HO_2^{\bullet}$) = −0.046 V vs NHE) [80]. The latter may further oxidize the dye directly or by the formation of radical intermediate species such as H_2O_2 (E^0 = +1.46 V vs NHE) [81]. However, the CB of BVO (−0.2 V vs. RHE) is not negative enough to promote the reaction of the electrons with adsorbed O_2 to generate $O_2^{\bullet-}$ radicals (E^0 ($O_2/O_2^{\bullet}$) = −0.33 V). On the other hand, the photogenerated holes at the VB of BVO are located at a more positive potential (+2.2 V vs. RHE calculated by considering the obtained CB energy level and the bandgap of the semiconductor) and can either directly oxidize the dye molecules or react with OH^- to produce hydroxyl radicals (E^0 ($OH^-/OH^{\bullet}$) = +1.9 V vs. NHE) [82].

Hence, the charge separation is facilitated by the concomitant presence of Pt and PtO_x at the surface of BVO by the formation of a dual metal/semiconductor junction with superior performance when compared only to BVO/Pt^0. Besides, the presence of oxidized platinum significantly increased the light absorption of the samples in the visible range as observed in Fig. 3. Therefore, the overall improved photoactivity is a result of the combination of two effects: (i) the improved light absorption and (ii) the better charge separation of the BVO/Pt/PtO_x photocatalyst.

4. Conclusions

In this study, BVO/Pt/PtO_x photocatalysts with different Pt^0/PtO_x ratios were successfully prepared using a controlled photoreduction/deposition process. A careful analysis of the oxidation state of Pt (Pt^0/Pt^{2+}/Pt^{4+}) cocatalyst deposited over monoclinic-BVO (0.75 %w/w) indicated that the PtO_x species perform better than Pt^0, leading to a 10-fold increase in the photodegradation rate constant under simulated solar irradiation and 58-fold increase under 420 nm LED irradiation, followed by an increase in apparent quantum yield as compared to pristine BVO by a factor of almost 4. Using an array of complementary analytical techniques, we attribute the enhanced photoactivity of BVO/Pt/PtO_x photocatalysts to their improved visible light absorption and better charge carrier separation than BVO, with Pt^0/PtO_x species functioning as traps for the photoexcited electrons in the CB of BVO. Finally, it is found that the concomitant presence of Pt^0 and PtO_x cocatalyst considerably enhances the photoactivity of BVO for the photodegradation of organic pollutants. The results reported herein may contribute to a better understanding of the role of metal oxidation states in the widely investigated metal/metal oxide/photocatalysts systems.

Author contributions

The manuscript was written through the contributions of all authors. All authors have approved the final version of the manuscript.

Funding

This study was financed in part by the Fundação Universidade Federal de Mato Grosso do Sul – UFMS/MEC – Brazil, by the Coordenação de Aperfeiçoamento de Pessoal de Nível Superior – Brasil (CAPES) – Finance Code 001, by the National Council for Scientific and Technological Development (CNPq) and The Foundation for Support to the Development of Teaching, Science and Technology of the State of Mato Grosso do Sul (FUNDECT).

CRediT authorship contribution statement

Luiz E. Gomes: Methodology, Investigation, Writing - original draft. **Adailton C. Nogueira:** Visualization, Investigation. **Marcio F. da Silva:** Investigation, Writing - original draft. **Luiz F. Plaça:** Investigation, Writing - original draft. **Lauro J.Q. Maia:** Investigation. **Renato V. Gonçalves:** Investigation, Writing - review & editing, Formal analysis. **Sajjad Ullah:** Writing - review & editing, Conceptualization, Formal analysis. **Sherdill Khan:** Investigation, Writing - review & editing, Formal analysis. **Heberton Wender:** Conceptualization, Supervision, Project administration, Investigation, Writing - review & editing, Funding acquisition.

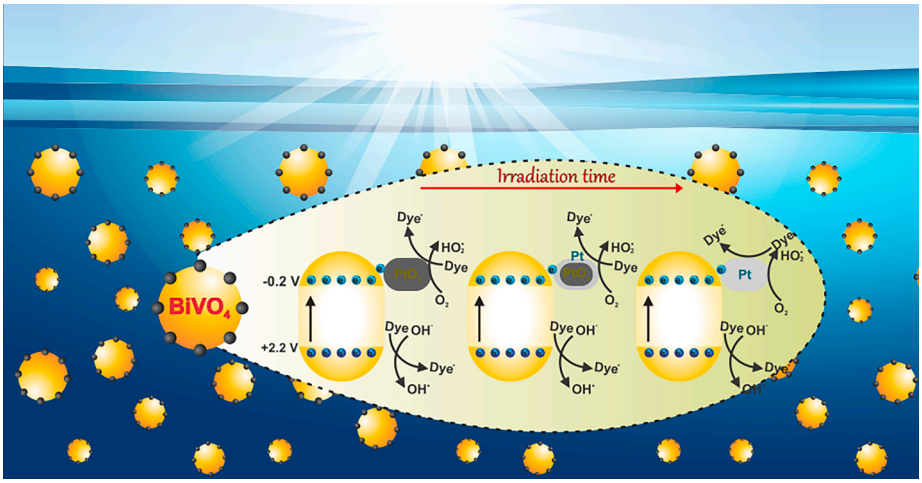

Fig. 8. Schematic representation of the photocatalytic mechanism of BVO/Pt/PtO_x photocatalysts.

Declaration of Competing Interest

The authors declare that they have no known competing financial interests or personal relationships that could have appeared to influence the work reported in this paper.

Acknowledgments

This work was partially supported by the Coordenação de Aperfeiçoamento de Pessoal de Nível Superior—Brasil (CAPES)—Finance Code 001 and Capes-PrInt program (grant numbers 88881.311921/2018-01 and 88887.311920/2018-00), by the National Council for Scientific and Technological Development (CNPq; process numbers 486342/2013-1, 427835/2016-0, 310066/2017-4 and 313300/2020-8), and by the Foundation for Support to the Development of Teaching, Science and Technology of the State of Mato Grosso do Sul (FUNDECT, process No. 23/200.247/2014). L.E.G. greatly appreciates the funding received from CAPES for his Ph.D. scholarship. S.K. and R.V.G. are thankful to FAPERGS (process no: 19/2551-0002287-5) and FAPESP (19/15434-2) to conduct the collaborative work approved in FAPESP-FAPERGS 2019 call. S.U. thanks Higher Education Commission, Pakistan (Project No. 9286) for financial assistance and the Federal University of Mato Grosso do Sul (UFMS) and São Paulo State University (UNESP) for the support and opportunity to work as visiting researcher. The authors also acknowledge Prof. Dr. Gleison A. Casagrande and Prof. Dr. Marco A. U. Martines for UV − vis diffuse reflectance and X-ray diffraction measurements, respectively.

Appendix A. Supplementary material

Supplementary data to this article can be found online at https://doi.org/10.1016/j.apsusc.2021.150773.

References

[1] WWAP (United Nations World Water Assessment Programme), The United Nations World Water Development Report, 2017. Wastewater. The Untapped Resource., Paris, UNESCO, 2017.
[2] H.G. Gorchev, G. Ozolins, WHO guidelines for drinking-water quality, WHO Chron. 38 (2011) 104–108, https://doi.org/10.1016/S1462-0758(00)00006-6.
[3] V. Katheresan, J. Kansedo, S.Y. Lau, Efficiency of various recent wastewater dye removal methods: A review, J. Environ. Chem. Eng. 6 (2018) 4676–4697, https://doi.org/10.1016/j.jece.2018.06.060.
[4] H.L. Tan, F.F. Abdi, Y.H. Ng, Heterogeneous photocatalysts: An overview of classic and modern approaches for optical, electronic, and charge dynamics evaluation, Chem. Soc. Rev. 48 (2019) 1255–1271, https://doi.org/10.1039/c8cs00882e.
[5] S. Ullah, E.P. Ferreira-Neto, A.A. Pasa, C.C.J. Alcântara, J.J.S. Acuña, S.A. Bilmes, M.L. Martínez Ricci, R. Landers, T.Z. Fermino, U.P. Rodrigues-Filho, Enhanced photocatalytic properties of core@shell SiO 2 @TiO 2 nanoparticles, Appl. Catal. B Environ. 179 (2015) 333–343, https://doi.org/10.1016/j.apcatb.2015.05.036.
[6] E.P. Ferreira-Neto, M.A. Worsley, U.P. Rodrigues-Filho, Towards thermally stable aerogel photocatalysts: TiCl4-based sol-gel routes for the design of nanostructured silica-titania aerogel with high photocatalytic activity and outstanding thermal stability, J. Environ. Chem. Eng. 7 (2019), 103425, https://doi.org/10.1016/j.jece.2019.103425.
[7] S. Ullah, E.P. Ferreira-Neto, C. Hazra, R. Parveen, H.D. Rojas-Mantilla, M. L. Calegaro, Y.E. Serge-Correales, U.P. Rodrigues-Filho, S.J.L. Ribeiro, Broad spectrum photocatalytic system based on BiVO4 and NaYbF4:Tm3+ upconversion particles for environmental remediation under UV-vis-NIR illumination, Appl. Catal. B Environ. 243 (2019) 121–135, https://doi.org/10.1016/j.apcatb.2018.09.091.
[8] S. Ullah, C. Hazra, E.P. Ferreira-Neto, T.C. Silva, U.P. Rodrigues-Filho, S.J. L. Ribeiro, Microwave-assisted synthesis of NaYF 4: Yb 3+ /Tm 3+ upconversion particles with tailored morphology and phase for the design of UV/NIR-active NaYF 4: Yb 3+ /Tm 3+ @TiO 2 core@shell photocatalysts, CrystEngComm. 19 (2017) 3465–3475, https://doi.org/10.1039/C7CE00809K.
[9] Y. Sang, H. Liu, A. Umar, Photocatalysis from UV/Vis to near-infrared light: Towards full solar-light spectrum activity, ChemCatChem 7 (2015) 559–573, https://doi.org/10.1002/cctc.201402812.
[10] S. Ullah, A.A. Fayeza, A. Khan, S.Q. Jan, E.P.F. Aain, Y.E. Neto, R. Serge-Correales, H. Parveen, U.P. Wender, S.J.L.R. Rodrigues-Filho, Enhanced photoactivity of BiVO4/Ag/Ag2O Z-scheme photocatalyst for efficient environmental remediation under natural sunlight and low-cost LED illumination, Colloids Surf. A Physicochem. Eng. Asp. 600 (2020), 124946, https://doi.org/10.1016/j.colsurfa.2020.124946.
[11] B. Baral, K.H. Reddy, K.M. Parida, Construction of M-BiVO4/T-BiVO4 isotype heterojunction for enhanced photocatalytic degradation of Norfloxacine and Oxygen evolution reaction, J. Colloid Interface Sci. 554 (2019) 278–295, https://doi.org/10.1016/j.jcis.2019.07.007.
[12] T.D. Nguyen, V.H. Nguyen, S. Nanda, D.V.N. Vo, V.H. Nguyen, T. Van Tran, L. X. Nong, T.T. Nguyen, L.G. Bach, B. Abdullah, S.S. Hong, T. Van Nguyen, BiVO4 photocatalysis design and applications to oxygen production and degradation of organic compounds: a review, Environ. Chem. Lett. (2020), https://doi.org/10.1007/s10311-020-01039-0.
[13] F. Stelo, N. Kublik, S. Ullah, H. Wender, Recent advances in Bi2MoO6 based Z-scheme heterojunctions for photocatalytic degradation of pollutants, J. Alloys Compd. 829 (2020), 154591, https://doi.org/10.1016/j.jallcom.2020.154591.
[14] T.S. Natarajan, K.R. Thampi, R.J. Tayade, Visible light driven redox-mediator-free dual semiconductor photocatalytic systems for pollutant degradation and the ambiguity in applying Z-scheme concept, Appl. Catal. B Environ. 227 (2018) 296–311, https://doi.org/10.1016/j.apcatb.2018.01.015.
[15] J. You, Y. Guo, R. Guo, X. Liu, A review of visible light-active photocatalysts for water disinfection: Features and prospects, Chem. Eng. J. 373 (2019) 624–641, https://doi.org/10.1016/j.cej.2019.05.071.
[16] L.E. Gomes, M.F. da Silva, R.V. Gonçalves, G. Machado, G.B. Alcantara, A.R. L. Caires, H. Wender, Synthesis and Visible-Light-Driven Photocatalytic Activity of Ta 4+ Self-Doped Gray Ta 2 O 5 Nanoparticles, J. Phys. Chem. C 122 (2018) 6014–6025, https://doi.org/10.1021/acs.jpcc.7b11822.
[17] R.V. Gonçalves, H. Wender, S. Khan, M.A. Melo, Photocatalytic water splitting by suspended semiconductor particles, in: Nanoenergy, Springer International Publishing, Cham, 2018, pp. 107–140, https://doi.org/10.1007/978-3-319-62800-4_3.
[18] A.C. Nogueira, L.E. Gomes, J.A.P. Ferencz, J.E.F.S. Rodrigues, R.V. Gonçalves, H. Wender, Improved Visible Light Photoactivity of $CuBi_2O_4$/CuO Heterojunctions for Photodegradation of Methylene Blue and Metronidazole, J. Phys. Chem. C 123 (2019) 25680–25690, https://doi.org/10.1021/acs.jpcc.9b06907.
[19] A.F. Feil, H. Wender, R.V. Gonçalves, Photovoltaic, photocatalytic application, and water splitting, 2016. https://doi.org/10.1002/9783527693283.ch13.
[20] A.P.P. da Rosa, R.P. Cavalcante, D.A. da Silva, L.D.M. da Silva, T.F. da Silva, F. Gozzi, E. McGlynn, A. Brady-Boyd, G.A. Casagrande, H. Wender, S.C. de Oliveira, A.M. Junior, H_2O_2-assisted photoelectrocatalytic degradation of Mitoxantrone using CuO nanostructured films: Identification of by-products and toxicity, Sci. Total Environ. 651 (2019), https://doi.org/10.1016/j.scitotenv.2018.10.173.
[21] H. Wender, R.V. Gonçalves, C.S.B. Dias, M.J.M. Zapata, L.F. Zagonel, E. C. Mendonça, S.R. Teixeira, F. Garcia, Photocatalytic hydrogen production of Co $(OH)_2$ nanoparticle-coated α-Fe_2O_3 nanorings, Nanoscale 5 (2013) 9310, https://doi.org/10.1039/c3nr02195e.
[22] S.S.M. Bhat, H.W. Jang, Recent Advances in Bismuth-Based Nanomaterials for Photoelectrochemical Water Splitting, ChemSusChem 10 (2017) 3001–3018, https://doi.org/10.1002/cssc.201700633.
[23] A. Malathi, V. Vasanthakumar, P. Arunachalam, J. Madhavan, M.A. Ghanem, A low cost additive-free facile synthesis of BiFeWO6/BiVO4 nanocomposite with enhanced visible-light induced photocatalytic activity, J. Colloid Interface Sci. 506 (2017) 553–563, https://doi.org/10.1016/j.jcis.2017.07.079.
[24] Z. Liu, H. Wang, G. Pan, J. Niu, P. Feng, Facile synthesis, structure and enhanced photocatalytic activity of novel BiOBr/Bi(C2O4)OH composite photocatalysts, J. Colloid Interface Sci. 486 (2017) 8–15, https://doi.org/10.1016/j.jcis.2016.09.052.
[25] K. Ding, B. Chen, Y. Li, Y. Zhang, Z. Chen, Comparative density functional theory study on the electronic and optical properties of BiMO4 (M = V, Nb, Ta), J. Mater. Chem. A. 2 (2014) 8294, https://doi.org/10.1039/c3ta15367c.
[26] Y. Liu, B. Huang, Y. Dai, X. Zhang, X. Qin, M. Jiang, M.H. Whangbo, Selective ethanol formation from photocatalytic reduction of carbon dioxide in water with BiVO4 photocatalyst, Catal. Commun. 11 (2009) 210–213, https://doi.org/10.1016/j.catcom.2009.10.010.
[27] M.J. Nalbandian, M. Zhang, J. Sanchez, Y.H. Choa, D.M. Cwiertny, N.V. Myung, Synthesis and optimization of BiVO4 and co-catalyzed BiVO4 nanofibers for visible light-activated photocatalytic degradation of aquatic micropollutants, J. Mol. Catal. A Chem. 404–405 (2015) 18–26, https://doi.org/10.1016/j.molcata.2015.04.003.
[28] H. Ullah, A.A. Tahir, T.K. Mallick, Structural and electronic properties of oxygen defective and Se-doped p -type BiVO 4 (001) thin film for the applications of photocatalysis, Appl. Catal. B Environ. 224 (2018) 895–903, https://doi.org/10.1016/j.apcatb.2017.11.034.
[29] P. Luan, J. Zhang, Stepping towards Solar Water Splitting: Recent Progress in Bismuth Vanadate Photoanodes, ChemElectroChem 6 (2019) 3227–3243, https://doi.org/10.1002/celc.201900398.
[30] L. Yun, Z. Yang, Z.-B. Yu, T. Cai, Y. Li, C. Guo, C. Qi, T. Ren, Synthesis of four-angle star-like CoAl-MMO/BiVO 4 p–n heterojunction and its application in photocatalytic desulfurization, RSC Adv. 7 (2017) 25455–25460, https://doi.org/10.1039/C7RA03012F.
[31] C. Regmi, D. Dhakal, S.W. Lee, Visible-light-induced Ag/BiVO 4 semiconductor with enhanced photocatalytic and antibacterial performance, Nanotechnology 29 (2018), 064001, https://doi.org/10.1088/1361-6528/aaa052.
[32] W. Zhao, J. Zhang, F. Zhu, F. Mu, L. Zhang, B. Dai, J. Xu, A. Zhu, C. Sun, D.Y. C. Leung, Study the photocatalytic mechanism of the novel Ag/p-Ag2O/n-BiVO4 plasmonic photocatalyst for the simultaneous removal of BPA and chromium(VI), Chem. Eng. J. 361 (2019) 1352–1362, https://doi.org/10.1016/j.cej.2018.12.181.

[33] J. Yang, D. Wang, H. Han, C. Li, Roles of Cocatalysts in Photocatalysis and Photoelectrocatalysis, Acc. Chem. Res. 46 (2013) 1900–1909, https://doi.org/10.1021/ar300227e.

[34] C.-H. Liao, C.-W. Huang, J.C.S. Wu, Hydrogen Production from Semiconductor-based Photocatalysis via Water Splitting, Catalysts 2 (2012) 490–516, https://doi.org/10.3390/catal2040490.

[35] D. Wang, Z.-P. Liu, W.-M. Yang, Revealing the Size Effect of Platinum Cocatalyst for Photocatalytic Hydrogen Evolution on TiO 2 Support: A DFT Study, ACS Catal. 8 (2018) 7270–7278, https://doi.org/10.1021/acscatal.8b01886.

[36] K. Wenderich, G. Mul, Methods, Mechanism, and Applications of Photodeposition in Photocatalysis: A Review, Chem. Rev. 116 (2016) 14587–14619, https://doi.org/10.1021/acs.chemrev.6b00327.

[37] Y. Lee, E. Kim, Y. Park, J. Kim, W.H. Ryu, J. Rho, K. Kim, Photodeposited metal-semiconductor nanocomposites and their applications, J. Mater. 4 (2018) 83–94, https://doi.org/10.1016/j.jmat.2018.01.004.

[38] J. Lv, H. Gao, H. Wang, X. Lu, G. Xu, D. Wang, Z. Chen, X. Zhang, Z. Zheng, Y. Wu, Controlled deposition and enhanced visible light photocatalytic performance of Pt-modified TiO2 nanotube arrays, Appl. Surf. Sci. 351 (2015) 225–231, https://doi.org/10.1016/j.apsusc.2015.05.139.

[39] S. Semlali, T. Pigot, D. Flahaut, J. Allouche, S. Lacombe, L. Nicole, Mesoporous Pt-TiO2 thin films: Photocatalytic efficiency under UV and visible light, Appl. Catal. B Environ. 150–151 (2014) 656–662, https://doi.org/10.1016/j.apcatb.2013.12.042.

[40] J. Zhang, Q. Zhang, Y. Yue, Y. Zhou, J. Shen, Z. Zhang, X. Wang, The effect of excitation wavelength on the photodeposition of Pt on polyhedron BiVO4 with exposing 010 and 110 facets for photocatalytic performance, Catal. Commun. 123 (2019) 100–104, https://doi.org/10.1016/j.catcom.2019.02.013.

[41] N. Murakami, N. Takebe, T. Tsubota, T. Ohno, Improvement of visible light photocatalytic acetaldehyde decomposition of bismuth vanadate/silica nanocomposites by cocatalyst loading, J. Hazard. Mater. 211–212 (2012) 83–87, https://doi.org/10.1016/j.jhazmat.2011.12.038.

[42] R. Li, H. Han, F. Zhang, D. Wang, C. Li, Highly efficient photocatalysts constructed by rational assembly of dual-cocatalysts separately on different facets of BiVO 4, Energy Environ. Sci. 7 (2014) 1369–1376, https://doi.org/10.1039/C3EE43304H.

[43] K.-E. Guima, L.E. Gomes, J. Alves Fernandes, H. Wender, C.A. Martins, Harvesting Energy from an Organic Pollutant Model Using a New 3D-Printed Microfluidic Photo Fuel Cell, ACS Appl. Mater. Interfaces 12 (2020) 54563–54572, https://doi.org/10.1021/acsami.0c14464.

[44] T. Liu, G. Tan, C. Zhao, C. Xu, Y. Su, Y. Wang, H. Ren, A. Xia, D. Shao, S. Yan, Enhanced photocatalytic mechanism of the Nd-Er co-doped tetragonal BiVO4 photocatalysts, Appl. Catal. B Environ. 213 (2017) 87–96, https://doi.org/10.1016/j.apcatb.2017.05.018.

[45] A. Malathi, J. Madhavan, M. Ashokkumar, P. Arunachalam, A review on BiVO4 photocatalyst: Activity enhancement methods for solar photocatalytic applications, Appl. Catal. A Gen. 555 (2018) 47–74, https://doi.org/10.1016/j.apcata.2018.02.010.

[46] J.K. Cooper, S. Gul, F.M. Toma, L. Chen, P.-A. Glans, J. Guo, J.W. Ager, J. Yano, I. D. Sharp, Electronic Structure of Monoclinic BiVO4, Chem. Mater. 26 (2014) 5365–5373, https://doi.org/10.1021/cm5025074.

[47] J. Yu, A. Kudo, Effects of structural variation on the photocatalytic performance of hydrothermally synthesized BiVO4, Adv. Funct. Mater. 16 (2006) 2163–2169, https://doi.org/10.1002/adfm.200500799.

[48] F.D. Hardcastle, I.E. Wachs, Determination of vanadium-oxygen bond distances and bond orders by Raman spectroscopy, J. Phys. Chem. 95 (1991) 5031–5041, https://doi.org/10.1021/j100166a025.

[49] Y. Li, H. Wang, Q. Feng, G. Zhou, Z.-S. Wang, Gold nanoparticles inlaid TiO2 photoanodes: a superior candidate for high-efficiency dye-sensitized solar cells, Energy Environ. Sci. 6 (2013) 2156, https://doi.org/10.1039/c3ee23971c.

[50] W.S. Li, Z.X. Shen, H.Y. Li, D.Z. Shen, X.W. Fan, Blue shift of Raman peak from coated TiO2 nanoparticles, J. Raman Spectrosc. 32 (2001) 862–865, https://doi.org/10.1002/jrs.773.

[51] S. Nikam, S. Joshi, Irreversible phase transition in BiVO 4 nanostructures synthesized by a polyol method and enhancement in photo degradation of methylene blue, RSC Adv. 6 (2016) 107463–107474, https://doi.org/10.1039/C6RA14700C.

[52] F. Fina, H. Ménard, J.T.S. Irvine, The effect of Pt NPs crystallinity and distribution on the photocatalytic activity of Pt–g-C 3 N 4, Phys. Chem. Chem. Phys. 17 (2015) 13929–13936, https://doi.org/10.1039/C5CP00560D.

[53] R.M. Mohamed, I.A. Mkhalid, A. Shawky, Facile synthesis of Pt–In2O3/BiVO4 nanospheres with improved visible-light photocatalytic activity, J. Alloys Compd. 775 (2019) 542–548, https://doi.org/10.1016/j.jallcom.2018.10.181.

[54] J.K. Cooper, S. Gul, F.M. Toma, L. Chen, Y.S. Liu, J. Guo, J.W. Ager, J. Yano, I. D. Sharp, Indirect bandgap and optical properties of monoclinic bismuth vanadate, J. Phys. Chem. C 119 (2015) 2969–2974, https://doi.org/10.1021/jp512169w.

[55] L. Chen, D. Meng, X. Wu, A. Wang, J. Wang, Y. Wang, M. Yu, In Situ Synthesis of V 4+ and Ce 3+ Self-Doped BiVO4/CeO 2 Heterostructured Nanocomposites with High Surface Areas and Enhanced Visible-Light Photocatalytic Activity, J. Phys. Chem. C 120 (2016) 18548–18559, https://doi.org/10.1021/acs.jpcc.6b04131.

[56] M.Q. Pham, T.M. Ngo, V.H. Nguyen, L.X. Nong, D.-V.N. Vo, T. Van Tran, T.-D. Nguyen, X.-T. Bui, T.D. Nguyen, Facile solvothermal synthesis of highly active monoclinic scheelite BiVO4 for photocatalytic degradation of methylene blue under white LED light irradiation, Arab. J. Chem. 13 (2020) 8388–8394, https://doi.org/10.1016/j.arabjc.2020.05.029.

[57] T.-Y. Huang, Y.-J. Chen, C.-Y. Lai, Y.-W. Lin, Synthesis, characterization, enhanced sunlight photocatalytic properties, and stability of Ag/Ag3PO4 nanostructure-sensitized BiPO4, RSC Adv. 5 (2015) 43854–43862, https://doi.org/10.1039/C5RA07101A.

[58] C.-K. Huang, T. Wu, C.-W. Huang, C.-Y. Lai, M.-Y. Wu, Y.-W. Lin, Enhanced photocatalytic performance of BiVO4 in aqueous AgNO3 solution under visible light irradiation, Appl. Surf. Sci. 399 (2017) 10–19, https://doi.org/10.1016/j.apsusc.2016.12.038.

[59] Y. Zhang, H. Fan, M. Li, H. Tian, Ag/BiPO4 heterostructures: synthesis, characterization and their enhanced photocatalytic properties, Dalt. Trans. 42 (2013) 13172, https://doi.org/10.1039/c3dt51056e.

[60] C. Xu, D. Lin, J.-N. Niu, Y.-H. Qiang, D.-W. Li, C.-X. Tao, Preparation of Ta-Doped TiO_2 Using Ta_2O_5 as the Doping Source, Chinese Phys. Lett. 32 (2015), 088102, https://doi.org/10.1088/0256-307X/32/8/088102.

[61] N. Barbero, D. Vione, Why Dyes Should Not Be Used to Test the Photocatalytic Activity of Semiconductor Oxides, Environ. Sci. Technol. 50 (2016) 2130–2131, https://doi.org/10.1021/acs.est.6b00213.

[62] A. Mishra, A. Panigrahi, P. Mal, S. Penta, G. Padmaja, G. Bera, P. Das, P. Rambabu, G.R. Turpu, Rapid photodegradation of methylene blue dye by rGO- V2O5 nano composite, J. Alloys Compd. 842 (2020), 155746, https://doi.org/10.1016/j.jallcom.2020.155746.

[63] A. Mohammadzadeh, M. Khoshghadam-Pireyousefan, B. Shokrianfard-Ravasjan, M. Azadbeh, H. Rashedi, M. Dibazar, A. Mostafaei, Synergetic photocatalytic effect of high purity ZnO pod shaped nanostructures with H2O2 on methylene blue dye degradation, J. Alloys Compd. 845 (2020), 156333, https://doi.org/10.1016/j.jallcom.2020.156333.

[64] H.L. Tan, X. Wen, R. Amal, Y.H. Ng, BiVO 4 010 and 110 Relative Exposure Extent: Governing Factor of Surface Charge Population and Photocatalytic Activity, J. Phys. Chem. Lett. 7 (2016) 1400–1405, https://doi.org/10.1021/acs.jpclett.6b00428.

[65] X. Lin, J. Hou, S. Jiang, Z. Lin, M. Wang, G. Che, A Z-scheme visible-light-driven Ag/Ag3PO4/Bi2MoO6 photocatalyst: synthesis and enhanced photocatalytic activity, RSC Adv. 5 (2015) 104815–104821, https://doi.org/10.1039/C5RA22110B.

[66] L. Zhang, Z. Dai, G. Zheng, Z. Yao, J. Mu, Superior visible light photocatalytic performance of reticular BiVO4 synthesized via a modified sol–gel method, RSC Adv. 8 (2018) 10654–10664, https://doi.org/10.1039/C8RA00554K.

[67] Y. Geng, P. Zhang, N. Li, Z. Sun, Synthesis of Co doped BiVO 4 with enhanced visible-light photocatalytic activities, J. Alloys Compd. 651 (2015) 744–748, https://doi.org/10.1016/j.jallcom.2015.08.123.

[68] A. Zulkifili, A. Fujiki, S. Kimijima, Flower-like BiVO4 Microspheres and Their Visible Light-Driven Photocatalytic Activity, Appl. Sci. 8 (2018) 216, https://doi.org/10.1016/S0731-7085(98)00261-1.

[69] Y. Xue, X. Wang, The effects of Ag doping on crystalline structure and photocatalytic properties of BiVO4, Int. J. Hydrogen Energy 40 (2015) 5878–5888, https://doi.org/10.1016/j.ijhydene.2015.03.028.

[70] V. Klimov, P.H. Bolivar, H. Kurz, Ultrafast carrier dynamics in semiconductor quantum dots, Phys. Rev. B 53 (1996) 1463–1467, https://doi.org/10.1103/PhysRevB.53.1463.

[71] D. Fang, X. Li, H. Liu, W. Xu, M. Jiang, W. Li, X. Fan, BiVO4-rGO with a novel structure on steel fabric used as high-performance photocatalysts, Sci. Rep. 7 (2017) 7979, https://doi.org/10.1038/s41598-017-07342-1.

[72] B. Xu, A. Zada, G. Wang, Y. Qu, Boosting the visible-light photoactivities of BiVO 4 nanoplates by Eu doping and coupling CeOx nanoparticles for CO2 reduction and organic oxidation, Sustain. Energy Fuels 3 (2019) 3363–3369, https://doi.org/10.1039/C9SE00409B.

[73] J. Ravensbergen, F.F. Abdi, J.H. van Santen, R.N. Frese, B. Dam, R. van de Krol, J. T.M. Kennis, Unraveling the Carrier Dynamics of BiVO4: A Femtosecond to Microsecond Transient Absorption Study, J. Phys. Chem. C 118 (2014) 27793–27800, https://doi.org/10.1021/jp509930s.

[74] W. Zhang, R. Li, X. Zhao, Z. Chen, A.W.K. Law, K. Zhou, A Cobalt-Based Metal-Organic Framework as Cocatalyst on BiVO4 Photoanode for Enhanced Photoelectrochemical Water Oxidation, ChemSusChem 11 (2018) 2710–2716, https://doi.org/10.1002/cssc.201801162.

[75] C. Liu, H. Luo, Y. Xu, W. Wang, Q. Liang, N. Mitsuzaki, Z. Chen, Cobalt–phosphate-modified Mo:BiVO 4 mesoporous photoelectrodes for enhanced photoelectrochemical water splitting, J. Mater. Sci. 54 (2019) 10670–10683, https://doi.org/10.1007/s10853-019-03658-7.

[76] M. Xie, Z. Zhang, W. Han, X. Cheng, X. Li, E. Xie, Efficient hydrogen evolution under visible light irradiation over BiVO4 quantum dot decorated screw-like SnO 2 nanostructures, J. Mater. Chem. A 5 (2017) 10338–10346, https://doi.org/10.1039/C7TA01415E.

[77] S. Wang, T. He, J.-H. Yun, Y. Hu, M. Xiao, A. Du, L. Wang, New Iron-Cobalt Oxide Catalysts Promoting BiVO4 Films for Photoelectrochemical Water Splitting, Adv. Funct. Mater. 28 (2018) 1802685, https://doi.org/10.1002/adfm.201802685.

[78] J.K. Kim, X. Shi, M.J. Jeong, J. Park, H.S. Han, S.H. Kim, Y. Guo, T.F. Heinz, S. Fan, C.L. Lee, J.H. Park, X. Zheng, Enhancing Mo:BiVO4 Solar Water Splitting with Patterned Au Nanospheres by Plasmon-Induced Energy Transfer, Adv. Energy Mater. 8 (2018) 1–9, https://doi.org/10.1002/aenm.201701765.

[79] D. Kong, J. Qi, D. Liu, X. Zhang, L. Pan, J. Zou, Ni-Doped BiVO4 with V4+ Species and Oxygen Vacancies for Efficient Photoelectrochemical Water Splitting, Trans. Tianjin Univ. 25 (2019) 340–347, https://doi.org/10.1007/s12209-019-00202-1.

[80] W. Liu, M. Wang, C. Xu, S. Chen, X. Fu, Ag3PO4/ZnO: An efficient visible-light-sensitized composite with its application in photocatalytic degradation of

Rhodamine B, Mater. Res. Bull. 48 (2013) 106–113, https://doi.org/10.1016/j.materresbull.2012.10.015.

[81] D.A. Armstrong, R.E. Huie, W.H. Koppenol, S.V. Lymar, G. Merényi, P. Neta, B. Ruscic, D.M. Stanbury, S. Steenken, P. Wardman, Standard electrode potentials involving radicals in aqueous solution: inorganic radicals (IUPAC Technical Report), Pure Appl. Chem. 87 (2015) 1139–1150, https://doi.org/10.1515/pac-2014-0502.

[82] M. Sun, Y. Su, C. Du, Q. Zhao, Z. Liu, Self-doping for visible light photocatalytic purposes: construction of SiO2/SnO2/SnO2:Sn2+ nanostructures with tunable optical and photocatalytic performance, RSC Adv. 4 (2014) 30820, https://doi.org/10.1039/C4RA04356A.